Mon. Not. R. Astron. Soc. **000**, 1–12 (2015) Printed 27 January 2021 (MN LATEX style file v2.2)

# Variability of the coronal line region in NGC 4151

Hermine Landt[1⋆†], Martin J. Ward[1†], Katrien C. Steenbrugge[2,3] and Gary J. Ferland[4,5]
[1] *Department of Physics, Durham University, South Road, Durham DH1 3LE, UK*
[2] *Instituto de Astronomía, Universidad Católica del Norte, Avenida Angamos 0610, 1270709 Antofagasta, Chile*
[3] *Department of Physics, University of Oxford, Keble Road, Oxford OX1 3RH, UK*
[4] *School of Mathematics and Physics, Queen's University of Belfast, Belfast BT7 1NN, Northern Ireland, UK*
[5] *Department of Physics and Astronomy, University of Kentucky, Lexington, KY 40506, USA*



Accepted . Received ; in original form

**ABSTRACT**

We present the first extensive study of the coronal line variability in an active galaxy. Our data set for the nearby source NGC 4151 consists of six epochs of quasi-simultaneous optical and near-infrared spectroscopy spanning a period of about eight years and five epochs of X-ray spectroscopy overlapping in time with it. None of the coronal lines showed the variability behaviour observed for the broad emission lines and hot dust emission. In general, the coronal lines varied only weakly, if at all. Using the optical [Fe VII] and X-ray O VII emission lines we estimate that the coronal line gas has a relatively low density of $n_e \sim 10^3$ cm$^{-3}$ and a relatively high ionisation parameter of $\log U \sim 1$. The resultant distance of the coronal line gas from the ionising source is about two light years, which puts this region well beyond the hot inner face of the obscuring dusty torus. The high ionisation parameter implies that the coronal line region is an independent entity rather than part of a continuous gas distribution connecting the broad and narrow emission line regions. We present tentative evidence for the X-ray heated wind scenario of Pier & Voit. We find that the increased ionising radiation that heats the dusty torus also increases the cooling efficiency of the coronal line gas, most likely due to a stronger adiabatic expansion.

**Key words:** galaxies: Seyfert – infrared: galaxies – X-rays: galaxies – quasars: emission lines – quasars: individual: NGC 4151

## 1 INTRODUCTION

In addition to the broad and narrow emission lines, the spectra of active galactic nuclei (AGN) display high-ionisation emission lines, the so-called coronal lines, which require energies $\gtrsim$ 100 eV to be excited. The coronal line region is believed to lie at distances from the central ionising source intermediate between those of the broad (BELR) and narrow emission line region (NELR) and to possibly coincide with the hot inner face of the circumnuclear, obscuring dusty torus (as first suggested by Pier & Voit 1995). Support for this assumption comes from the fact that the coronal lines have higher critical densities for collisional deexcitation than the low-ionisation narrow emission lines ($n_e \sim 10^7 - 10^{10}$ cm$^{-3}$), their profiles tend to have full widths at half maxima (FWHM) intermediate between those of the broad and narrow emission lines (FWHM$\sim$ 500 − 1500 km s$^{-1}$; e.g., Penston et al. 1984; Appenzeller & Oestreicher 1988; Erkens et al. 1997; Rodríguez-Ardila et al. 2002, 2011) and the emission from this region is often extended but much less so than that from the low-ionisation NELR (on scales of $\sim$ 80 − 150 pc; e.g., Prieto et al. 2005; Müller Sánchez et al. 2006; Müller-Sánchez et al. 2011; Mazzalay et al. 2013). Coronal lines are observed with smilar frequency in both types of AGN (Osterbrock 1977; Koski 1978), but type 1 AGN have stronger coronal line emission relative to their low-ionisation narrow lines than type 2 AGN (Murayama & Taniguchi 1998). Therefore, it is likely that the coronal line region has two components, one compact and one spatially extended, with only the latter remaining unobscured by the dusty torus in type 2 AGN.

The high ionisation potentials of the coronal lines can be produced either in a hot, collisionally ionised plasma, as is the case for the solar corona from which these lines have their name, or in a gas photoionised by the hard continuum of the

⋆ E-mail: hermine.landt@durham.ac.uk
† Visiting Astronomer at the Infrared Telescope Facility, which is operated by the University of Hawaii under Cooperative Agreement no. NNX-08AE38A with the National Aeronautics and Space Administration, Science Mission Directorate, Planetary Astronomy Program.

AGN. In the first case, the electron temperatures would be of the order of $T_e \approx 10^6$ K and in the second case much lower ($T_e \sim 10^4 - 10^5$ K). Currently, photoionisation is favoured, since for most AGN the observed flux ratios between different coronal lines can be reproduced within a factor of $\sim 2-3$ by these models (Oliva et al. 1994; Ferguson et al. 1997), whereas the temperature of the hot plasma would need to be fine-tuned within a very narrow range (Oliva et al. 1994). In any case, the coronal line region is most likely dust free, since strong emission from refractory elements such as iron, silicium and calcium are observed, which would be severly reduced in a dusty environment.

The coronal lines are often blueshifted relative to the low-ionisation narrow lines (e.g., Penston et al. 1984; Erkens et al. 1997; Rodríguez-Ardila et al. 2002), which indicates that the coronal line gas is in outflow. However, as Mullaney et al. (2009) concluded for the source Ark 564, the potential coronal line emitting clouds must have undergone acceleration to the observed velocities prior to these lines being produced, i.e. they have reached their terminal velocity against the opposing drag and gravitational forces. Then, given also the similar estimated physical conditions and location, it has been proposed that the partly ionised gas that produces the O VII and O VIII absorption lines and edges seen in the soft X-ray spectra of many AGN, i.e., the so-called 'warm absorber', produces also the coronal lines in its (colder) outer regions (Netzer 1993; Erkens et al. 1997; Porquet et al. 1999). In this wind model for the coronal line region, a considerable contribution from shock ionisation is expected.

The most stringent constraints on the properties of the coronal line emitting region could come from variabililty studies, in particular if the variability of several coronal lines can be compared with each other and with that of other AGN components such as the BELR and the X-ray continuum. However, mainly due to the weakness of these emission lines and also lack of data, very few studies of this kind have been attempted so far. Veilleux (1988) did the only systematic study of the coronal line variability. In his sample of $\sim 20$ AGN he found firm evidence that both the [Fe VII] $\lambda$6087 and [Fe X] $\lambda$6375 emission lines varied (during a period of a few years) for only one source (NGC 5548) and tentative evidence for another seven sources (including NGC 4151). Then, within a general optical variability campaign on the source Mrk 110 lasting for half a year, Kollatschny et al. (2001) reported strong [Fe X] variations. More recently, follow-up optical spectroscopy of a handful of objects with unusually prominent coronal lines selected from the Sloan Digital Sky Survey (SDSS) showed that in half of them the coronal lines strongly faded (by factors of $\sim 2-10$), making these sources candidates for stellar tidal disruption events (Komossa et al. 2009; Yang et al. 2013).

In this paper, we present the first extensive study of the coronal line variability in an AGN. Our data set for the nearby, well-known source NGC 4151 ($z = 0.0033$) is unprecedented in that it includes six epochs of quasi-simultaneous optical and near-IR spectroscopy spanning a period of $\sim 8$ years and five epochs of X-ray spectroscopy overlapping in time with it. Furthermore, the observations in each wavelength were performed with the same telescope and set-up. This paper is organised as follows. In Section 2, we present the data and measurements. In Section 3, we discuss the observed variability behaviour of the near-IR, optical and X-ray coronal lines, for which we seek an interpretation in the context of the location of and excitation mechanism for the coronal line emission region in Section 4. Finally, in Section 5, we summarise our main results and present our conclusions. Throughout this paper we have assumed cosmological parameters $H_0 = 70$ km s$^{-1}$ Mpc$^{-1}$, $\Omega_{\rm M} = 0.3$, and $\Omega_\Lambda = 0.7$.

## 2 THE DATA AND MEASUREMENTS

### 2.1 Near-IR and optical spectroscopy

We have six epochs of quasi-simultaneous (within 3-14 days) near-IR and optical spectroscopy for NGC 4151 (see Tables 1 and 2). The near-IR spectroscopy was obtained with the SpeX spectrograph (Rayner et al. 2003) at the NASA Infrared Telescope Facility (IRTF), a 3 m telescope on Mauna Kea, Hawai'i, in the short cross-dispersed mode (SXD, $0.8-2.4$ $\mu$m). All data except those from 2010 were obtained through a slit of $0.8 \times 15''$ giving an average spectral resolution of full width at half maximum (FWHM) $\sim 400$ km s$^{-1}$. A narrower slit of $0.3 \times 15''$ was used for the 2010 epoch. The four epochs spanning the years $2004-2007$ are our own data and were presented in Landt et al. (2008) and Landt et al. (2011). The near-IR spectra from 2002 and 2010 were discussed by Riffel et al. (2006) and Schnülle et al. (2013), respectively. The optical spectra were obtained with the FAST spectrograph (Fabricant et al. 1998) at the Tillinghast 1.5 m telescope on Mt. Hopkins, Arizona, using the 300 l/mm grating and a $3''$ long-slit. This set-up resulted in a wavelength coverage of $\sim 3720 - 7515$ Å and an average spectral resolution of FWHM $\sim 330$ km s$^{-1}$. The slit was rotated to the parallactic angle only for the January 2006 epoch, however, except for the 2004 data, all spectra were observed at a very low airmass (sec $z \sim 1.05$). The May 2004 spectrum was observed at an airmass of sec $z \sim 1.3$ and so the flux loss due to atmospheric differential refraction is expected to be $\sim 20\%$ at the observed wavelength of [Fe VII] $\lambda$3759 relative to that at wavelengths $\geqslant 5000$ Å (Filippenko 1982). The January 2006 data were discussed in Landt et al. (2008), whereas all other optical spectra were retrieved from the FAST archive.

We have measured the fluxes of the strongest near-IR and optical coronal lines by integrating the observed profiles over the local continuum, i.e. we have not assumed a specific line shape. In the near-IR, we have measured two sulfur lines and two silicon lines, namely, [S VIII] $\lambda$9911, [S IX] 1.252$\mu$m, [Si VI] 1.965$\mu$m and [Si X] 1.430$\mu$m (see Table 1). Two of these emission lines are blended, namely, [S IX] with [Fe II] 1.257$\mu$m, and [Si VI] with $H_2$ 1.957$\mu$m. In these cases, we have assumed a Gaussian profile in the deblending procedure. In the optical, we have measured four iron emission lines, namely, [Fe VII] $\lambda$3759, [Fe VII] $\lambda$5159, [Fe VII] $\lambda$5721 and [Fe VII] $\lambda$6087 (see Table 2). We have considered also [Fe X] $\lambda$6375, but this line is extremely weak in NGC 4151 and makes up only $\sim 15\%$ of the total blend with [O I] $\lambda$6364 (Pelat et al. 1987). We do not observe significant variability in the flux of the entire blend, which constrains the [Fe X] variability to below a factor of $\sim 2$.

Since both the near-IR and optical spectra were obtained in non-photometric sky conditions, we study in the

**Table 1.** Near-IR emission line fluxes and ratios

| Observation Date | [S III] $\lambda$9531 (erg/s/cm$^2$) | [S III] $\lambda$9069 (erg/s/cm$^2$) | [S III]/ [S III] | [S VIII] $\lambda$9911 (erg/s/cm$^2$) | [S III]/ [S VIII] | [S IX] 1.252$\mu$m (erg/s/cm$^2$) | [S III]/ [S IX] |
|---|---|---|---|---|---|---|---|
| 2002 Apr 23 | (7.61±0.09)e−13 | (2.66±0.02)e−13 | 2.86±0.04 | (2.49±0.21)e−14 | 30.6±2.6 | (2.44±0.12)e−14 | 31.2±1.6 |
| 2004 May 23 | (1.06±0.02)e−12 | (3.89±0.08)e−13 | 2.73±0.08 | (5.35±0.60)e−14 | 19.8±2.3 | (2.64±0.28)e−14 | 40.2±4.3 |
| 2006 Jan 8 | (1.17±0.01)e−12 | (4.40±0.06)e−13 | 2.66±0.04 | (3.81±0.26)e−14 | 30.7±2.1 | (3.41±0.14)e−14 | 34.3±1.4 |
| 2006 Jun 12 | (9.97±0.10)e−13 | (3.85±0.07)e−13 | 2.59±0.05 | (3.38±0.19)e−14 | 29.5±1.7 | (3.54±0.12)e−14 | 28.2±1.0 |
| 2007 Jan 24 | (8.17±0.14)e−13 | (2.79±0.06)e−13 | 2.93±0.08 | (3.09±0.38)e−14 | 26.4±3.3 | (3.01±0.29)e−14 | 27.1±2.6 |
| 2010 Feb 27 | (8.89±0.15)e−13 | (2.98±0.06)e−13 | 2.98±0.08 | (4.00±0.36)e−14 | 22.2±2.0 | (3.31±0.19)e−14 | 26.9±1.6 |
| Observation Date | [S III] $\lambda$9531 (erg/s/cm$^2$) | [Si VI] 1.965$\mu$m (erg/s/cm$^2$) | [S III]/ [Si VI] | [Si X] 1.430$\mu$m (erg/s/cm$^2$) | [S III]/ [Si X] | Pa$\beta$ (erg/s/cm$^2$) | [S III]/ Pa$\beta$ |
| 2002 Apr 23 | (7.61±0.09)e−13 | (6.75±0.23)e−14 | 11.3±0.4 | (4.75±0.22)e−14 | 16.0±0.8 | (9.22±0.09)e−13 | 0.825±0.013 |
| 2004 May 23 | (1.06±0.02)e−12 | (9.91±0.51)e−14 | 10.7±0.6 | (6.23±0.58)e−14 | 17.0±1.6 | (7.59±0.24)e−13 | 1.397±0.053 |
| 2006 Jan 8 | (1.17±0.01)e−12 | (8.56±0.33)e−14 | 13.7±0.5 | (4.51±0.19)e−14 | 25.9±1.1 | (1.11±0.01)e−12 | 1.054±0.014 |
| 2006 Jun 12 | (9.97±0.10)e−13 | (7.59±0.20)e−14 | 13.1±0.4 | (6.26±0.50)e−14 | 15.9±1.3 | (9.19±0.13)e−13 | 1.085±0.018 |
| 2007 Jan 24 | (8.17±0.14)e−13 | (6.58±0.18)e−14 | 12.4±0.4 | (4.18±0.24)e−14 | 19.6±1.2 | (8.04±0.26)e−13 | 1.016±0.037 |
| 2010 Feb 27 | (8.89±0.15)e−13 | (7.72±0.68)e−14 | 11.5±1.0 | (5.79±0.77)e−14 | 15.4±2.1 | (1.64±0.01)e−12 | 0.542±0.010 |

**Table 2.** Optical emission line fluxes and ratios

| Observation Date | [O III] $\lambda$5007 (erg/s/cm$^2$) | [O III] $\lambda$4959 (erg/s/cm$^2$) | [O III]/ [O III] | [Fe VII] $\lambda$3759 (erg/s/cm$^2$) | [O III]/ [Fe VII] | [Fe VII] $\lambda$5159 (erg/s/cm$^2$) | [O III]/ [Fe VII] |
|---|---|---|---|---|---|---|---|
| 2002 Apr 11 | (8.52±0.03)e−12 | (2.96±0.03)e−12 | 2.88±0.03 | (7.87±1.38)e−14 | 108.3±19.0 | (4.23±0.57)e−14 | 201.4±27.0 |
| 2004 May 28 | (1.18±0.01)e−11 | (4.60±0.04)e−12 | 2.57±0.02 | (1.85±0.25)e−13 | 63.8±8.7 | (6.60±0.73)e−14 | 178.8±19.7 |
| 2006 Jan 5 | (1.17±0.01)e−11 | (3.92±0.02)e−12 | 2.99±0.02 | (9.66±0.58)e−14 | 121.1±7.3 | (5.36±0.21)e−14 | 218.3±8.7 |
| 2006 May 29 | (9.80±0.04)e−12 | (3.86±0.03)e−12 | 2.54±0.02 | (9.25±1.36)e−14 | 106.0±15.6 | (5.34±0.60)e−14 | 183.5±20.7 |
| 2007 Feb 9 | (1.46±0.01)e−11 | (5.09±0.04)e−12 | 2.87±0.03 | (7.45±1.20)e−14 | 196.0±31.6 | (5.32±0.40)e−14 | 274.4±20.9 |
| 2010 Feb 18 | (9.79±0.03)e−12 | (3.14±0.02)e−12 | 3.12±0.03 | (6.82±1.15)e−14 | 143.6±24.3 | (3.46±0.29)e−14 | 283.0±24.1 |
| Observation Date | [O III] $\lambda$5007 (erg/s/cm$^2$) | [Fe VII] $\lambda$5721 (erg/s/cm$^2$) | [O III]/ [Fe VII] | [Fe VII] $\lambda$6087 (erg/s/cm$^2$) | [O III]/ [Fe VII] | H$\alpha$ (erg/s/cm$^2$) | [O III]/ H$\alpha$ |
| 2002 Apr 11 | (8.52±0.03)e−12 | (8.67±0.68)e−14 | 98.3±7.7 | (1.19±0.10)e−13 | 71.6±5.7 | (1.43±0.01)e−11 | 0.596±0.005 |
| 2004 May 28 | (1.18±0.01)e−11 | (9.75±0.81)e−14 | 121.0±10.1 | (1.91±0.11)e−13 | 61.8±3.6 | (1.47±0.01)e−11 | 0.803±0.005 |
| 2006 Jan 5 | (1.17±0.01)e−11 | (8.73±0.39)e−14 | 134.0±6.0 | (1.64±0.07)e−13 | 71.3±3.2 | (1.64±0.01)e−11 | 0.713±0.003 |
| 2006 May 29 | (9.80±0.04)e−12 | (8.32±0.68)e−14 | 117.8±9.7 | (1.26±0.11)e−13 | 77.8±6.8 | (1.46±0.01)e−11 | 0.671±0.005 |
| 2007 Feb 9 | (1.46±0.01)e−11 | (9.93±0.62)e−14 | 147.0±9.1 | (1.73±0.08)e−13 | 84.4±4.1 | (1.41±0.01)e−11 | 1.035±0.007 |
| 2010 Feb 18 | (9.79±0.03)e−12 | (7.25±0.56)e−14 | 135.0±10.4 | (1.39±0.09)e−13 | 70.4±4.4 | (1.89±0.02)e−11 | 0.518±0.005 |

following the temporal changes of the coronal lines in relative rather than absolute flux. In particular, we scale the coronal line emission to that of a strong, forbidden *low-ionisation* emission line that is unblended and observed in the same spectrum. The emission region that produces the low-ionisation narrow lines is believed to be located at large enough distances from the central ionising source for its flux to remain constant on timescales of decades. We have scaled the near-IR and optical coronal lines to the [S III] $\lambda$9531 and [O III] $\lambda$5007 emission lines, respectively.

The error estimates on the line fluxes are crucial for assessing the significance of the coronal line variability. The data are of relatively high signal-to-noise ratio (continuum $S/N \gtrsim 50-100$) and, therefore, the main sources of measurement errors are of a subjective nature, namely, the placement of the local continuum and related to this the setting of the extension of the emission line. These are problematic in most cases since the lines in question sit on top of broad emission lines, namely, [S III] $\lambda$9531 in the blue wing of Pa$\epsilon$, [S VIII] in the blue wing of Pa$\delta$, [S IX] in the blue wing of Pa$\beta$, [Si VI] in the red wing of Br$\delta$, [O III] $\lambda$5007 in the red wing of H$\beta$ and [Fe X] in the blue wing of H$\alpha$. Therefore, in order to estimate meaningful uncertainties for the measured line fluxes we have considered in addition to the statistical errors due to the data quality also profile comparisons. These were done in velocity space between the scaling lines [S III] $\lambda$9531 and [O III] $\lambda$5007 and the coronal lines and helped us judge the influence of the continuum placement on the recovery of the true line profile. The total estimated $1\sigma$ uncertainties for all measured line fluxes are listed in Tables 1 and 2. They are $\sim 1-2\%$ for the strongest lines and $\sim 3-15\%$ for the weakest ones.

In order to further constrain the significance of the observed coronal line variability, we have considered the two extreme cases of where no variability and the highest variability are expected. For both scaling lines we observe also the other emission line that is emitted from the same upper level, namely, [S III] $\lambda$9069 and [O III] $\lambda$4959. Their observed ratios, which should be close to the theoretical values of [S III] $\lambda$9531/[S III] $\lambda$9069=2.58 and [O III] $\lambda$5007/[O III] $\lambda$4959=2.92 (Kramida et al. 2013), are not expected to vary and so their observed variability sets a

**Table 3.** Near-IR continuum fluxes and optical coronal line ratios

| Observation Date | $\lambda f_{1\mu m}$ (erg/s/cm$^2$) | $\lambda f_{1\mu m}$/ [S III] | $\lambda f_{2.1\mu m}$ (erg/s/cm$^2$) | $\lambda f_{2.1\mu m}$/ [S III] | $T_{dust}$ (K) | [Fe VII] $\lambda$6087/ [Fe VII] $\lambda$3759 | [Fe VII] $\lambda$5159/ [Fe VII] $\lambda$6087 |
|---|---|---|---|---|---|---|---|
| 2002 Apr 23 | (8.57±0.03)e−11 | 112.6±1.5 | (1.22±0.01)e−10 | 160.3±1.9 | 1316 | 1.512±0.290 | 0.355±0.055 |
| 2004 May 23 | (7.79±0.25)e−11 | 73.5±2.9 | (1.18±0.01)e−10 | 111.3±2.7 | 1281 | 1.032±0.153 | 0.346±0.043 |
| 2006 Jan 8 | (9.34±0.07)e−11 | 79.8±0.7 | (1.62±0.01)e−10 | 138.5±1.0 | 1328 | 1.698±0.127 | 0.327±0.020 |
| 2006 Jun 12 | (6.67±0.07)e−11 | 66.9±1.0 | (1.50±0.01)e−10 | 150.5±1.7 | 1278 | 1.362±0.233 | 0.424±0.061 |
| 2007 Jan 24 | (5.12±0.28)e−11 | 62.7±3.6 | (1.04±0.01)e−10 | 127.3±2.4 | 1231 | 2.322±0.390 | 0.308±0.028 |
| 2010 Feb 27 | (2.18±0.01)e−10 | 245.2±4.4 | (3.47±0.01)e−10 | 390.3±6.6 | 1393 | 2.038±0.367 | 0.249±0.026 |

**Table 4.** XMM-*Newton* archival observations

| No. | Observation date and time | Exp. (ks) | Obs ID | Campaign |
|---|---|---|---|---|
| 1 | 2000:12:21 16:45:30 | 33 | 0112310101 | 2000 Dec |
| 2⋆ | 2000:12:21 14:21:13 | 8 | 0112310501 | |
| 3 | 2000:12:22 10:42:18 | 62 | 0112830201 | |
| 4 | 2000:12:22 02:53:42 | 23 | 0112830501 | |
| 5⋆ | 2000:12:22 04:02:18 | 5 | 0112830601 | |
| 6 | 2003:05:25 08:37:56 | 19 | 0143500101 | 2003 May |
| 7 | 2003:05:26 20:35:02 | 19 | 0143500201 | |
| 8 | 2003:05:27 15:16:51 | 19 | 0143500301 | |
| 9 | 2006:05:16 06:21:42 | 40 | 0402660101 | 2006 May |
| 10 | 2006:11:29 17:20:13 | 53 | 0402660201 | 2006 Nov |
| 11 | 2011:05:11 15:20:09 | 16 | 0657840101 | 2011 May |
| 12 | 2011:06:12 13:36:34 | 16 | 0657840201 | |

⋆ no EPIC data

lower threshold for the significance of the coronal line variability. Then, we have measured the fluxes of the two prominent broad emission lines Pa$\beta$ (in the near-IR) and H$\alpha$ (in the optical). Since the BELR is expected to be the most variable of any AGN emission line region, the observed variability of these broad lines gives an estimate of the maximum value that can be reached within the current data set. These results are also listed in Tables 1 and 2.

In addition to the emission lines, we have measured in the near-IR spectra the continuum fluxes at the rest-frame wavelengths of $\sim$ 1 $\mu$m and $\sim$ 2.1 $\mu$m (see Table 3). As we have shown in Landt et al. (2011), the former is dominated by the accretion disc flux, which is believed to be the main source of ionising radiation in AGN and so the driver of the observed variability, whereas the latter is emitted from the hot dust component of the obscuring torus, which, if its location indeed coincides with that of the coronal line region, should have a variability response similar to it. Furthermore, we have derived the hot dust temperature from blackbody fits to the near-IR spectral continuum as described in Landt et al. (2011) and list it also in Table 3. In Section 4, we will compare these values to the optical coronal line ratios [Fe VII] $\lambda$6087/[Fe VII] $\lambda$3759 and [Fe VII] $\lambda$5159/[Fe VII] $\lambda$6087, which are suitable indicators of the gas temperature and density (Nussbaumer et al. 1982; Keenan & Norrington 1987), respectively (listed in Table 3).

### 2.2 X-ray spectroscopy

Between December 2000 and June 2011, the time period that overlaps with our optical and near-IR observations, there were five observational campaigns with XMM-*Newton* on NGC 4151 (see Table 4). We have reduced these archival data sets using the standard tasks in the XMM-*Newton* SAS software (version 13.5.). All the X-ray spectral analysis was done using the `SPEX` software[1] (Kaastra et al. 1996). We have assumed solar abundances as given by Lodders & Palme (2009) and corrected all spectra for a Galactic column density of $2\times10^{24}$ m$^2$. Three of the campaigns have multiple observations, with two of them (2000 December and 2003 May) extending over a period of 2-3 days and another one (2011 May) spanning a period of a month. Since the X-ray emission lines are not expected to vary on days to weeks timescales (Detmers et al. 2008, 2009) and in order to improve the $S/N$ ratio, we have stacked the individual RGS spectra into one spectrum per campaign. We have treated the May 16 and November 29, 2006, observations separately, since the time span between them is about half a year. The longest and shortest observations are for the December 2000 and May 2011 campaigns with total exposure times of 131 ks and 32 ks, respectively.

In the X-rays, NGC 4151 is classified as an obscured Seyfert 1 galaxy, i.e. the soft X-ray emission is heavily obscured by an absorber. However, this absorption is not as deep as that observed for Seyfert 2 galaxies and a very weak continuum is present. This absorber is different from the warm absorber detected in the ultraviolet (UV) and X-ray spectra of $\sim$50% of Seyfert 1 galaxies (Crenshaw et al. 2003). It has a much larger column density, outflow velocity and velocity broadening, is variable on much shorter timescales and only partially covers the X-ray continuum source. In order to differentiate this absorber from the warm absorber, we follow Kaastra et al. (2014) and will call it 'the obscurer'. Since the soft and hard X-ray continuua as well as the properties of the obscurer, such as its column density, covering factor and potentially also the ionisation, are known to be variable on day timescales or less, we have not combined the EPIC pn spectra, but fitted them separately.

The presence of the obscurer in NGC 4151 allows us to study in detail the X-ray emission lines, which would otherwise be swamped by the high continuum flux. However, the obscurer also complicates the analysis, in particular the continuum fitting, since the absorption is so deep that the individual absorption lines blend and create a pseudo-continuum. Decomposing the total absorption into obscurer and warm absorber and characterising each individually is not possible without prior knowledge of the ionisation structure of the warm absorber. This, however, is not known for

[1] http://www.sron.nl/spex

**Table 5.** X-ray emission line and continuum fluxes

| Observation Epoch | O VII f 0.561 keV (ph/s/cm$^2$) | O VII i 0.569 keV (ph/s/cm$^2$) | O VII r 0.574 keV (ph/s/cm$^2$) | O VIII $\alpha$ 0.654 keV (ph/s/cm$^2$) | Ne IX f 0.905 keV (ph/s/cm$^2$) |
|---|---|---|---|---|---|
| 2000 Dec | (5.05±0.17)e−04 | (0.70±0.09)e−04 | (1.51±0.10)e−04 | (1.47±0.06)e−04 | (0.59±0.04)e−04 |
| 2003 May | (5.10±0.21)e−04 | (0.43±0.09)e−04 | (1.36±0.13)e−04 | (2.02±0.06)e−04 | (0.56±0.04)e−04 |
| 2006 May | (4.70±0.21)e−04 | (0.78±0.11)e−04 | (1.55±0.13)e−04 | (1.59±0.08)e−04 | (0.45±0.08)e−04 |
| 2006 Nov | (3.89±0.24)e−04 | (0.55±0.31)e−04 | (1.49±0.34)e−04 | (1.60±0.08)e−04 | (0.49±0.07)e−04 |
| 2011 May | (5.63±0.95)e−04 | (0.98±0.58)e−04 | (1.80±0.62)e−04 | (1.87±0.28)e−04 | (0.87±0.16)e−04 |
| Observation Epoch | N VI f 0.420 keV (ph/s/cm$^2$) | N VII $\alpha$ 0.500 keV (ph/s/cm$^2$) | C VI $\alpha$ 0.368 keV (ph/s/cm$^2$) | $f_{2-10\mathrm{keV}}$ (erg/s/cm$^2$) | |
| 2000 Dec | (1.51±0.09)e−04 | (0.87±0.05)e−04 | (2.66±0.13)e−04 | (6.37±0.06)e−11 | |
| 2003 May | (1.59±0.10)e−04 | (0.97±0.06)e−04 | (2.91±0.15)e−04 | (3.05±0.24)e−10 | |
| 2006 May | (1.27±0.13)e−04 | (0.94±0.08)e−04 | (3.10±0.22)e−04 | (7.91±0.08)e−11 | |
| 2006 Nov | (1.23±0.14)e−04 | (0.73±0.09)e−04 | (2.43±0.22)e−04 | (1.37±0.01)e−10 | |
| 2011 May | (1.05±0.48)e−04 | (0.84±0.28)e−04 | (2.63±0.74)e−04 | (1.55±0.05)e−10 | |

NGC 4151 since it has never been observed in an unobscured state. However, for the Seyfert 1 galaxy NGC 5548 we have high-quality X-ray spectra in both the unobscured (Steenbrugge et al. 2003, 2005; Detmers et al. 2009) and obscured state (Kaastra et al. 2014). Thus, we have assumed in our X-ray analysis that the obscurer in NGC 4151 has the same structure as that in NGC 5548, albeit being deeper. This is supported by the fact that the C IV absorption lines observed in the *Hubble Space Telescope* (HST) UV spectra of NGC 4151 (Kraemer et al. 2006) and NGC 5548 (Kaastra et al. 2014) have a similar width and blueshift.

Following the approach chosen by Kaastra et al. (2014) for NGC 5548, we first fitted the May 2003 spectrum, since it is the least absorbed state and allows for a better determination of the warm absorber and obscurer components. Each warm absorber or obscurer component was fitted with an `xabs` model. Then, using their results for NGC 5548, we assumed that the obscurer has two components, one close to or neutral with a lower covering factor and another medium-ionised with a much larger covering factor. From the UV spectrum of NGC 4151 we know that there are at least six warm absorber components with different velocities (see Fig. 2 in Kraemer et al. 2006), but their ionisation structure is undetermined by these data. We have added a further four warm absorber components (each an `xabs` model) with different ionisation parameters. Although the ionisation parameter of the warm absorber and obscurer can overlap, we only allowed higher ionization parameters for the warm absorber. The free parameters in the fit were the hydrogen column density and ionisation parameter, and in the case of the obscurer also the covering factor. The outflow velocity and velocity broadening were left at the standard values since they cannot be constrained. Finally, we assumed that the narrow emission lines are unaffected by the obscurer and warm absorber.

We modelled the continuum as observed with EPIC-pn with a reflection component and a comptoionisation model, which dominate the hard X-rays, and added a modified blackbody in the soft X-ray regime. The fit also includes, but the parameters are frozen, the best fit model for the emission lines, both narrow and broad, and the radiative recombination continua as determined from the RGS spectra. The Fe K$\alpha$ and K$\beta$ lines, which can only be studied with the EPIC instruments, were fitted as Gaussians. Both lines are unresolved. We fit the spectra in the $0.3-10$ keV energy range and used the option of optimal binning available in `SPEX`. This gives an acceptable fit to the EPIC-pn spectra. However, due to the heavy absorption, there is a certain degeneracy between the normalisation and temperature of the modified blackbody, the hydrogen column density, ionisation parameter and for the obscurer also the covering factor, of the absorption components and the normalisation of the emission lines and radiative recombination continua (frozen in the EPIC pn fit). In Table 5, we list the fluxes and $1\sigma$ errors for the eight strongest X-ray coronal lines, mainly from oxygen but also from nitrogen, carbon and neon, and the unabsorbed $2-10$ keV continuum fluxes. The errors on the line fluxes are $\sim 3-10\%$ for the strongest lines and $\sim 10-20\%$ for the weakest lines. The errors for the May 2011 observing campaign are much larger on all measurements ($\sim 20-60\%$).

## 3 THE VARIABILITY BEHAVIOUR

### 3.1 The near-IR and optical coronal lines

In the $\sim 8$ year period sampled by the near-IR and optical spectroscopy the ionising flux of the accretion disc, which is assumed to be the main driver for the variability of the broad line, coronal line and hot dust emission regions, decreased by a factor of $\sim 2$ in the first five years and increased by a factor of $\sim 4$ in the following three years (see Fig. 1). We note that the flux increase of $\sim 9\%$ observed between the May 2004 and January 2006 epochs is consistent with zero once the deviations from the theoretical value of the [S III] $\lambda$9531/[S III] $\lambda$9069 ratios measured in these spectra are taken into account ($\sim 5.5\%$ and $\sim 2.9\%$, respectively). The Pa$\beta$ broad line region and hot dust emission responded to the accretion disc variability in a similar way (see Figs. 2 and 1, respectively); their flux decreased in the first two years by $\sim 70\%$ and $\sim 50\%$, respectively, and then continuously increased for the next six years by a factor of $\sim 3$ and $\sim 4$, respectively. We note that the flux decrease of $\sim 20\%$ observed for the hot dust emission between the June 2006 and January 2007 epochs is similar to the deviation from the theoretical value measured for the [S III] $\lambda$9531/[S III] $\lambda$9069 ratio in the latter spectrum ($\sim 13.3\%$). The flux of the H$\alpha$

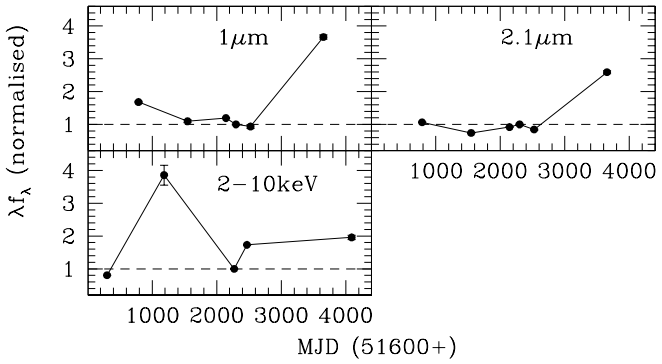


**Figure 1.** The variability of the continuum fluxes at rest-frame wavelengths of $\sim 1$ $\mu$m (sampling the accretion disc), $\sim 2.1$ $\mu$m (sampling the hot dust emission) and in the energy range 2 − 10 keV (related to the accretion disc). The near-IR continuum fluxes were divided by the [S III] $\lambda$9531 line flux and all continuum fluxes were normalised to the value of the May/June 2006 epoch. We plot $1\sigma$ error bars.

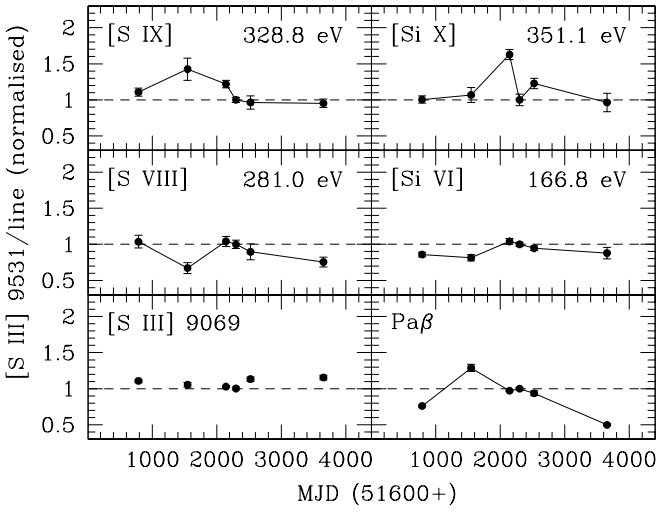


**Figure 2.** The variability of the near-IR coronal lines in the period April 2002 - February 2010. For comparison, we show also the [S III] $\lambda$9069 narrow line and Pa$\beta$ broad line, which are expected not to vary and to vary maximally, respectively. The [S III] $\lambda$9531/[S III] $\lambda$9069 flux ratios were normalised to the theoretical value, whereas those between [S III] $\lambda$9531 and the other lines were normalised to the value of the June 2006 epoch. We plot $1\sigma$ error bars. The ionisation potentials of the coronal lines are given at the top right.

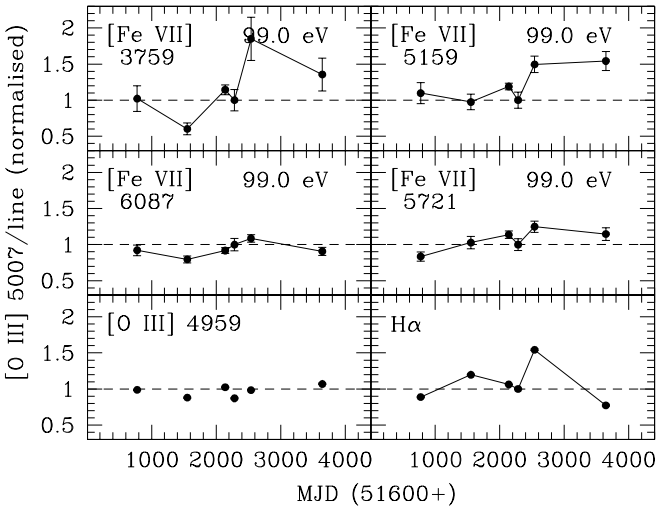


**Figure 3.** Same as Fig. 2 for the optical coronal lines. For comparison, we show also the [O III] $\lambda$4959 narrow line and H$\alpha$ broad line, which are expected not to vary and to vary maximally, respectively.

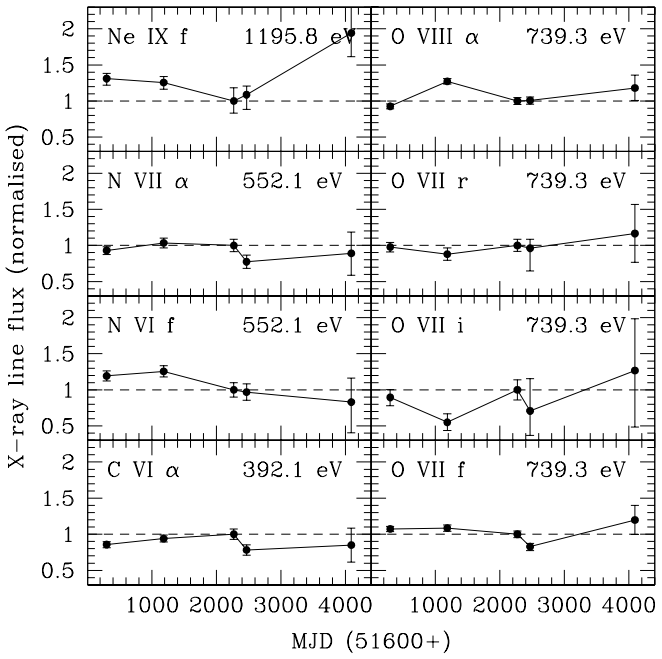


**Figure 4.** The variability of the X-ray coronal lines in the period December 2000 - May 2011. The flux values were normalised to the value of the May 2006 epoch. We plot $1\sigma$ error bars. The ionisation potentials of the coronal lines are given at the top right.

broad line region also decreased in the first two years (by $\sim$ 35%) and increased in the next two years (by $\sim$ 20%), but then it decreased for a short period (between June 2006 and January 2007 by $\sim$ 54%) before it increased strongly for the last three years (by a factor of $\sim 2$; see Fig. 3). The intermittent flux decrease might be caused by a reddening event, which we discuss further in Section 4.

The variability response of the near-IR coronal lines in the four year period between January 2006 and February 2010 is similar to that of the Pa$\beta$ broad line region and hot dust emission, with a trend that the higher the ionisation potential, the higher the flux increase, namely, $\sim$ 69% for the [Si X] line, $\sim$ 28% for the [S IX] line, $\sim$ 38% for the [S VIII] line, and no significant variability for the [Si VI] line (see Fig. 2). In the first two years sampled by the data significant variability is observed only for the [S VIII] line; a flux *increase* by $\sim$ 54%. Then, for all but the [S IX] line, a flux decrease (instead of the increase seen for the broad line

region and hot dust emission) is observed between May 2004 and January 2006, namely, $\sim 52\%$ for the [Si X] line, $\sim 55\%$ for the [S VIII] line, and $\sim 28\%$ for the [Si VI] line.

Between April 2002 and January 2006 we detect significant variability for only one optical coronal line, namely, [Fe VII] $\lambda$3759, which behaves similar to the [S VIII] line (see Fig. 3); a flux increase (by $\sim 70\%$) followed by a flux decrease (by $\sim 90\%$). The flux decrease observed for the H$\alpha$ broad line region between June 2006 and January 2007 is clearly evident for the [Fe VII] $\lambda$3759, [Fe VII] $\lambda$5159 and [Fe VII] $\lambda$5721 lines; their fluxes changed by $\sim 85\%$, $\sim 50\%$ and $\sim 25\%$, respectively. If we consider the period of January 2006 to January 2007 instead, we observe a similar behaviour also for the [Fe VII] $\lambda$6087 line; its flux decreased by $\sim 18\%$. In the following three years the [Fe VII] $\lambda$6087 line flux increased by $\sim 20\%$, as observed for the broad line region and hot dust emission, whereas none of the other optical coronal lines varied significantly.

### 3.2 The X-ray coronal lines

In the $\sim 10.5$ year period sampled by the X-ray spectroscopy the unabsorbed $2-10$ keV continuum flux, which is assumed to be produced by the central ionising source and so to be linked to the accretion disc flux, increased by a factor of $\sim 5$ in the first two and a half years, decreased by a factor of $\sim 4$ in the next three years, and then increased again by a factor of $\sim 2$ in the next five years.

The variability response of the three forbidden X-ray coronal lines in the period between November 2006 and May 2011 is similar to that of the near-IR coronal lines and that of the Pa$\beta$ broad line region and hot dust emission, and again with a trend that the higher the ionisation potential, the higher the flux increase, namely, a factor of $\sim 2$ for the Ne IX f line, $\sim 45\%$ for the O VII f line and no significant variability for the N VI f line (see Fig. 4). Then, whereas the flux stayed roughly constant in the first two and half years sampled by the data, similar to the near-IR coronal lines, a flux decrease (instead of the increase seen for the broad line region and hot dust emission) is observed in the period between May 2003 and May 2006 for the O VII f line (by $\sim 31\%$) and the N VI f line (by $\sim 30\%$).

In the entire time period sampled by the data no significant variability is observed for the recombination line O VII r, whereas the intercombination line O VII i showed strong variability between December 2000 and May 2006, with a flux decrease by $\sim 62\%$ followed by a flux increase by $\sim 82\%$. No significant variability is observed for the O VII i line after May 2006, which could be due to the relatively large errors on the line flux for the following two observing epochs. The O VIII $\alpha$ line showed also significant variability between December 2000 and May 2006, but contrary to the O VII i line, its flux increased first (by $\sim 37\%$) and then decreased (by $\sim 27\%$). Also for this line there is no significant variability after May 2006. The variability response of the two permitted X-ray coronal lines with the highest ionisation potentials is similar to that of the O VII f line; a significant flux decrease is observed for the N VII $\alpha$ line only between May 2003 and November 2006 (by $\sim 34\%$) and for the C VI $\alpha$ line only between May 2006 and November 2006 (by $\sim 28\%$).

## 4 THE ORIGIN OF THE CORONAL LINE EMISSION REGION

The current understanding is that the coronal line region in AGN is dust-free, photoionised and located beyond the BELR at distances from the central ionising source similar to those of the hot inner face of the obscuring dusty torus. In this scenario, we expect to observe the coronal line flux to vary similarly to that of the broad lines and hot dust emission but on timescales longer and shorter than the former and latter, respectively. With our data set we can test the first premise, although its sparse time sampling does not allow us to measure any variability timescales.

The variability behaviour observed for the broad lines and hot dust emission in the period covered by our data is both similar and simple; a flux decrease of $\sim 40-70\%$ in the first two years followed by a strong flux increase by a factor of $\sim 2-4$ in the following six years. *This variability behaviour is not observed for any of the coronal lines.* In general, the coronal lines varied weakly if at all, with the largest flux change observed to be only $\sim 50-90\%$ in a period of about two years. Specifically, in the first four years sampled by the data, the coronal lines either did not vary significantly or showed the opposite behaviour to that of the broad lines and hot dust emission. In the last four years sampled by the data, only the coronal lines with the highest ionisation potentials showed a variability behaviour similar to that of the broad lines and hot dust emission, but with a much reduced amplitude (a lower flux change per year by a factor of $\sim 2-4$), whereas the flux of the coronal lines with relatively low ionisation potentials remained unchanged.

The characteristic variability response time is a sum of the light travel time, which depends mainly on the location of the emission region, and the recombination time, which depends strongly on the gas number density:

$$\tau_{\rm var} = \tau_{\rm lt} + \tau_{\rm rec} \quad (1)$$

Therefore, the low variability amplitude observed for the coronal line gas in NGC 4151 indicates either that it is located well beyond the broad line region and dusty torus or that it has a relatively low density or both. In the following, we use published results from high-spatial resolution imaging campaigns at near-IR, optical and X-ray frequencies and apply plasma diagnostics to our own data in order to constrain both the location and gas number density of the coronal line emission region.

### 4.1 Published high-spatial resolution observations

NGC 4151 has a well-measured hydrogen broad line region lag time of about a week (Zu et al. 2011) and a hot dust lag time varying between $\sim 30-70$ days (Koshida et al. 2014). One possible explanation for the fact that the coronal line region reacted much weaker to changes in the ionising flux than both the broad line and hot dust emission regions is that it is located much further out than them.

High-spatial resolution observations of NGC 4151 in the near-IR were presented by several authors. Storchi-Bergmann et al. (2009) used the Gemini Near-IR Integral Field Spectrograph (NIFS) on December 2006 to image the source in the $0.94-2.42$ $\mu$m wavelength range with a spatial resolution of $0.12-0.16$ arcsec, which corre-

sponds to $\approx 8-10$ pc at the source. Their contour maps of the [S VIII] and [S IX] coronal lines show a compact, spatially unresolved region. Müller-Sánchez et al. (2011) and Iserlohe et al. (2013) used the Keck OH Suppressing InfraRed Imaging Spectrograph (OSIRIS) on March 2006 and February/May 2005, respectively, to image the source in the $1.96-2.38$ $\mu$m wavelength range with a spatial resolution of $0.08-0.11$ arcsec, which corresponds to $\approx 5-7$ pc at the source. Their contour maps of the [Si VI] coronal line show a bright nucleus containing $\sim 70\%$ of the total emission, which is surrounded by low-level extended emission up to $\approx 50-80$ pc.

The source NGC 4151 was observed with the Space Telescope Imaging Spectrograph (STIS) on-board the *Hubble Space Telescope (HST)* on several occasions. These observations span a large optical wavelength range and have a spatial resolution of 0.1 arcsec, corresponding to $\approx 7$ pc at the source. Nelson et al. (2000) presented measurements of the [Fe VII] $\lambda$3759, [Fe VII] $\lambda$5721 and [Fe VII] $\lambda$6087 coronal line fluxes along the slit at two different position angles for observations taken between January and June 1998. Along one of the position angles (P.A. 70°), the [Fe VII] $\lambda$3759 emission was spatially unresolved, but the [Fe VII] $\lambda$5721 and [Fe VII] $\lambda$6087 emission lines showed extents of up to $\approx 70-100$ pc from the nucleus. Along the other position angle (P.A. 221°), all three [Fe VII] emission lines were spatially resolved, however, with much lesser extents of $\approx 20-50$ pc from the nucleus. In all cases, the total [Fe VII] emission was dominated by the nuclear flux.

Wang et al. (2011b,a) analysed the deep exposure of NGC 4151 taken in March 2008 with the Advanced CCD Imaging Spectrometer (ACIS) on-board the *Chandra* X-ray observatory. By applying subpixel event repositioning and binning techniques they were able to improve the effective spatial resolution of the ACIS images to better than 0.4 arcsec, which corresponds to $\approx 25$ pc at the source. Their emission line maps of O VII (f, i and r), O VIII $\alpha$ and Ne IX (f, i and r) show an extremely bright nucleus surrounded by extended emission in the inner region of $\approx 130$ pc, and for the O VII and O VIII emission lines also very low-level emission ($\sim 10\%$ of the total flux) up to $\approx 2$ kpc.

In summary, high-spatial resolution observations of NGC 4151 show that whereas its coronal line emission region is extended in some chemical species, the total flux that our variability study is most sensitive to is dominated by the unresolved nuclear region. This region can currently be constrained by direct imaging only to $\lesssim 5$ pc (or $\lesssim 15$ light years), which is much larger than the measured distance of the hot dust emission of $\sim 2$ light months.

### 4.2 Plasma diagnostics

For the optical and X-ray coronal line gas we can estimate the density using the three iron lines [Fe VII] $\lambda$3759, [Fe VII] $\lambda$5159 and [Fe VII] $\lambda$6087 and the three lines from the helium-like ion of oxygen O VII f, O VII i and O VII r, respectively. Using the plasma simulation code CLOUDY (last described by Ferland et al. 1998), we have generated a temperature versus density grid for the collisionally excited [Fe VII] lines (see Fig. 5) and a ionisation parameter versus density grid for the O VII lines (see Fig. 6). The iron collision strengths were taken from

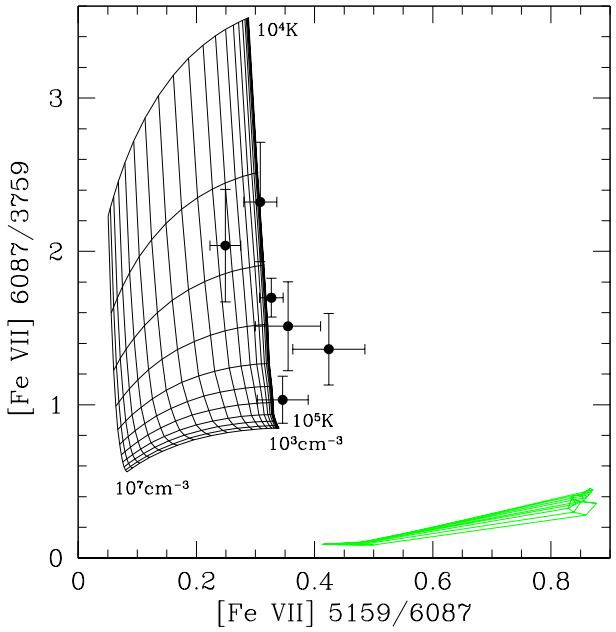


**Figure 5.** The observed optical coronal line ratios [Fe VII] $\lambda$6087/$\lambda$3759 versus [Fe VII] $\lambda$5159/$\lambda$6087, overlaid with curves of constant temperature ($\log T = 4, 4.1, 4.2, ...5$ K) and constant number density ($\log n_e = 3, 3.2, 3.4, ...7$ cm$^{-3}$) for the case of photoionisation equilibrium. The case of collisional ionisation equilibrium is shown in green. We plot $1\sigma$ error bars.

Witthoeft & Badnell (2008). For the photoionisation simulations we have approximated the incident radiation field with the mean AGN spectral energy distribution derived by Mathews & Ferland (1987). As discussed by previous studies, the line ratios [Fe VII] $\lambda$6087/$\lambda$3759 and [Fe VII] $\lambda$5159/$\lambda$6087 are suitable indicators of temperature and density, respectively (Nussbaumer et al. 1982; Keenan & Norrington 1987), whereas the X-ray line ratios O VII (f+i)/r (the so-called G ratio) and O VII f/i (the so-called R ratio) trace the ionisation parameter, which is directly related to the kinetic gas temperature, and density, respectively, for a given column density (Porquet & Dubau 2000; Porter & Ferland 2007). We assumed the cases of either photoionisation or collisional ionisation equilibrium.

The measurements for NGC 4151 in both Figs. 5 and 6 give two main consistent results; the coronal line gas is photoionised rather than collisionally ionised and its density appears to be relatively low. In the case of the optical coronal line gas, if we assume that the gas density did not change with time, four of the observing epochs constrain it to $n_e \sim 10^3$ cm$^{-3}$ within $\sim 1\sigma$, whereas the two observing epochs January and June 2006 reach this value within $\sim 2\sigma$. If we assume the gas density changed between observing epochs, at the $2\sigma$ level it varied between $n_e \sim 10^{5.2}$ cm$^{-3}$ and $n_e \lesssim 10^3$ cm$^{-3}$, since at the low-density limit the grid contours fall on top of each other. The highest density value is about two orders of magnitude lower than the critical density of [Fe VII] of $n_{\rm crit} \sim 3 \times 10^7$ cm$^{-3}$. We get a similar result for the X-ray coronal line gas; assuming the gas density did not change with time, two observing epochs (November 2006 and May 2011) constrain it to $n_e \sim 10^3$ cm$^{-3}$ within $\sim 1\sigma$,

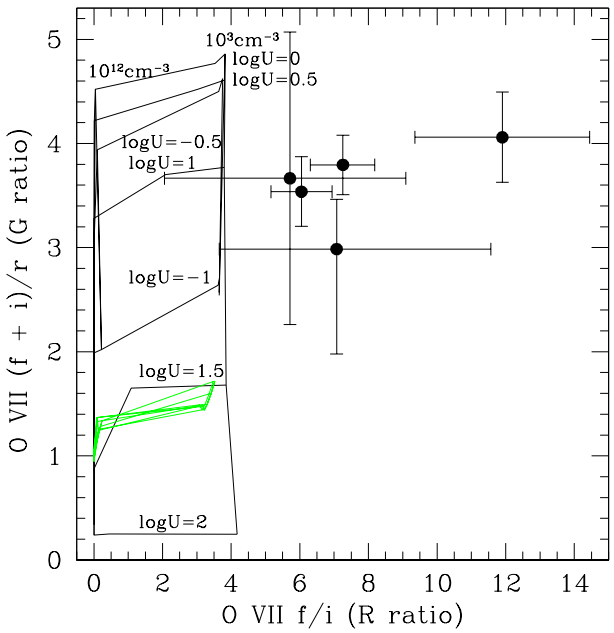


**Figure 6.** The observed X-ray coronal line ratios O VII (f+i)/r (G ratio) versus O VII f/i (R ratio), overlaid with curves of constant ionisation parameter ($\log U = -1, -0.5, 0, ...2$) for two constant number densities ($n_e = 10^3$ cm$^{-3}$ and $n_e = 10^{12}$ cm$^{-3}$) and a fixed column density of $N_{\rm H} = 10^{21}$ cm$^{-2}$, assuming photoionisation equilibrium. The case of collisional ionisation equilibrium is shown in green. We plot $1\sigma$ error bars.

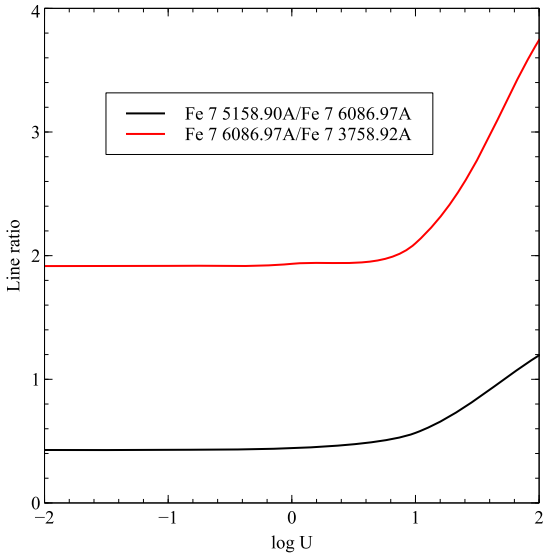


**Figure 7.** The effect of continuum pumping on the optical coronal line ratios [Fe VII] $\lambda$6087/$\lambda$3759 (red solid line) and [Fe VII] $\lambda$5159/$\lambda$6087 (black solid line) in dependence of the ionisation parameter. The gas is assumed to have a temperature of $T_e = 10^{4.25}$ K and a number density of $n_e = 10^3$ cm$^{-3}$.

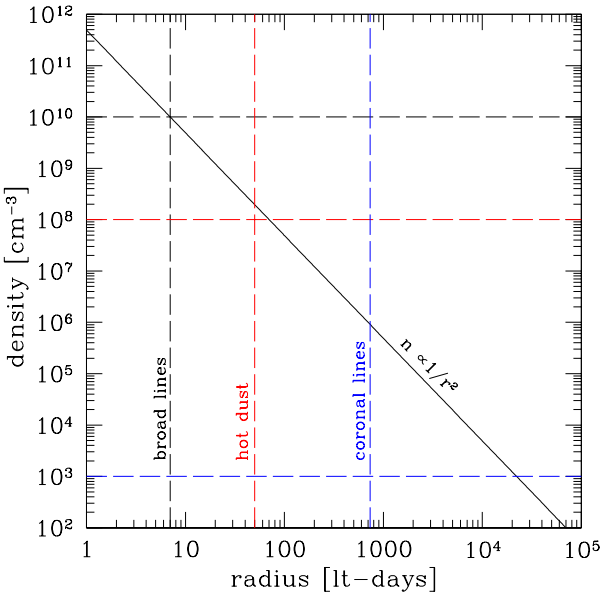


**Figure 8.** The density run with radius calculated for the relationship $n \propto r^{-2}$ (black solid line) and scaled to the observed lag time and expected gas number density for the hydrogen broad line region in NGC 4151 (black dashed lines). The red dashed lines show the observed lag time and expected gas number density for the hot dust. The estimated density and distance of the coronal line region are indicated by the blue dashed lines.

whereas three observing epochs reach this value within $\sim 3\sigma$. If we assume the density changed between observing epochs, at the $2\sigma$ level it varied between $n_e \sim 10^{12}$ cm$^{-3}$ (i.e. close to the critical density) and $n_e \lesssim 10^3$ cm$^{-3}$, since at the low-density limit the grid contours fall on top of each other.

It is worth noting that all measured O VII ratios and most of the [Fe VII] ratios are to the right of the theoretical grids. In the case of O VII, there are no known uncertainties in the atomic data and adding a contribution from collisionally ionised plasma would not increase the R ratios, which are observed to be much higher than predicted by theory. Similarly high R ratios are found also in other AGN, e.g., R = 5.50 for Mrk 3 (Pounds & Page 2005) and R = 7.73 for NGC 1068 (Kraemer et al. 2015). However, in the case of [Fe VII], it is possible that some contribution from fluorescence is present given the relatively low gas density in combination with the large ionisation parameter we estimate below. The large number of permitted Fe VII lines in the far-UV can be pumped by the continuum, which, when radiatively decaying, will add to the lower levels responsible for the [Fe VII] lines studied here. Fig. 7 shows the importance of this effect for a gas of number density $n_e = 10^3$ cm$^{-3}$ in dependence of the ionisation parameter. At a ionisation parameter of $\log U \sim 1$ the expected increase in the [Fe VII] $\lambda$5159/$\lambda$6087 ratio is a factor of $\sim 1.5$, whereas the increase in the [Fe VII] $\lambda$6087/$\lambda$3759 ratio is only $\sim 10\%$.

From Fig. 5 we estimate a temperature of $T \sim 10^{4.25}$ K$\sim$ 18000 K for the $Fe^{6+}$ gas. At this temperature, the recombination time is:

$$\tau_{\rm rec} \approx \frac{1}{n_e \cdot 1.70 \times 10^{-10}} \ {\rm s}, \qquad (2)$$

which for a gas number density of $n_e = 10^3$ cm$^{-3}$ results in $\tau_{\rm rec} \approx 5.9 \times 10^6$ s $\approx$ 2.2 months. We note that we have used the total recombination coefficient, i.e. the sum of the radiative and dielectronic recombination coefficients, which was calculated based on the atomic data presented by Gu et al. (2006). This value differs from that listed in

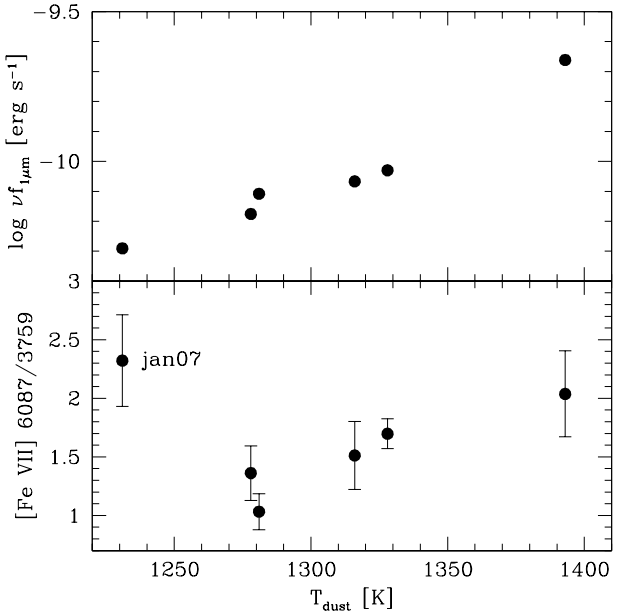


**Figure 9.** The top and bottom panels show the continuum flux at rest-frame wavelength of $\sim 1$ $\mu$m (sampling the accretion disc) and the optical coronal line ratio [Fe VII] $\lambda$6087/$\lambda$3759, which is a suitable indicator of the gas temperature (the higher its value, the lower the temperature; see Fig. 5), respectively, versus the hot dust blackbody temperature.

Osterbrock & Ferland (2006) by about an order of magnitude, since the latter represented only the radiative recombination coefficient. From Fig. 6, we constrain the ionisation parameter for all X-ray observing epochs at the $1\sigma$ level to $\log U \sim 1$. Then, using the unabsorbed X-ray luminosity of $L_{2-10\mathrm{keV}} \sim 10^{43}$ erg s$^{-1}$ resulting from our fits for the highest-flux epoch as a proxy for the ionising luminosity producing O VII and the best-fit X-ray spectral slope of this epoch of $\Gamma \sim 1.43$ to estimate the mean ionising photon energy, the calculated distance of the coronal line region from the central ionising source for the above gas density is $\tau_{\mathrm{lt}} \sim 730$ light days $\sim 2.0$ light years. This value, which is far below the resolution provided by current direct imaging results (see Section 4.1), puts this region well beyond the hot inner face of the obscuring dusty torus. Together our estimates of $\tau_{\mathrm{rec}}$ and $\tau_{\mathrm{lt}}$ give a characteristic variability response time of $\tau_{\mathrm{var}} \approx 2.2$ years, which is consistent with our main observational result that the coronal line gas emission in NGC 4151 has varied in an observing period of $\sim 8-11$ years, but only weakly so relative to the variability observed for the broad lines and hot dust emission.

But how can we explain our other observational result that during half the time period covered by the data the variable coronal lines showed the opposite trend to the flux changes observed for the broad lines and hot dust emission, i.e. their emission decreased instead of increased? In order to answer this question, we first need to understand how the coronal line region in NGC 4151 relates to the BELR, the dusty torus and the low-ionisation NELR. For this purpose, we have plotted in Fig. 8 the run of gas number density with radius for a relationship $n \propto r^{-2}$, which keeps the ionisation parameter constant. We have scaled this relationship to the observed lag time for the hydrogen BELR (of about a week) and the typical density for this emission region of $n_e \sim 10^{10}$ cm$^{-3}$. This scaling gives at the observed lag time for the hot dust (of $\sim 50$ days) a density of $n_e \sim 10^8$ cm$^{-3}$, which is consistent with what is currently assumed for the dusty torus material. From the relationship in Fig. 8, we see that, at the density estimated for the coronal line region of $n_e \sim 10^3$ cm$^{-3}$, a ionisation parameter typical of the BELR is reached at distances from the ionising source of $\sim 55$ light years, which is in the range observed for the spatially resolved low-ionisation NELR. However, the coronal line region in NGC 4151 appears to require a much higher ionisation parameter than the hydrogen BELR for its lines to form, which, at a given radius, can only be achieved by a considerable drop in density. Therefore, it seems that the coronal line region is not part of a continuous gas distribution but rather an independent entity.

One possibility proposed by Pier & Voit (1995) is that the coronal line region is a layer on the inner part of the dusty torus that becomes an efficient coronal line emitter only when evaporated in an X-ray heated wind. If this scenario applies to NGC 4151, the wind will have undergone adiabatic expansion from its launch location at the inner face of the torus until the gas density and distance from the ionising source are optimal to give the required high ionisation parameter. In the process, the coronal line gas will have cooled. In Fig. 9, we present tentative evidence for this scenario. In the bottom panel, we compare the temperature of the coronal line gas as measured by the line ratio [Fe VII] $\lambda$6087/[Fe VII] $\lambda$3759 (the higher its value, the lower the gas temperature; see Fig. 5) with that of the hot dust. We find that the two temperatures behave in opposite ways; the temperature of the coronal line gas is high when the hot dust temperature is low and vice versa. Only the data from January 2007 is an exception to this trend and might indicate a reddening event, which could also explain the decreased flux of the H$\alpha$ broad line relative to that of the Pa$\beta$ broad line for this epoch (see Section 3.1). In the top panel of Fig. 9, we show the continuum flux at rest-frame wavelength of $\sim 1$ $\mu$m, which samples the accretion disc luminosity, versus the hot dust temperature. A clear correlation is apparent, which indicates that the change in temperature for the hot dust is due to direct heating by the central ionising source. Therefore, the increased AGN radiation that heats the dusty torus appears to increase the cooling efficiency of the coronal line gas. In the scenario of Pier & Voit (1995), the dusty clouds will be evaporated in an X-ray heated wind more efficiently for higher AGN luminosities, which will lead to an increase in mass outflow rate but also to a stronger adiabatic expansion and so cooling.

## 5 SUMMARY AND CONCLUSIONS

We have presented the first extensive study of the coronal line variability in an AGN. Our data set for the nearby, well-known source NGC 4151 is unprecedented in that it includes six epochs of quasi-simultaneous optical and near-IR spectroscopy spanning a period of $\sim 8$ years and five epochs of X-ray spectroscopy overlapping in time with it. Our main results are as follows.

(i) The variability behaviour observed for the broad

emission lines and hot dust emission was not mirrored in any of the coronal lines. The coronal lines varied only weakly, if at all. Specifically, in the first four years sampled by the data, the coronal lines either did not vary significantly or showed the opposite behaviour to that of the broad lines and hot dust emission, whereas after that only the coronal lines with the highest ionisation potentials showed a variability behaviour similar to that of the broad lines and hot dust emission, but with a much reduced amplitude (a lower flux change per year by a factor of $\sim 2-4$).

(ii) We have applied plasma diagnostics to the optical [Fe VII] and X-ray O VII emission lines in order to constrain the gas number density, temperature and ionisation parameter of the coronal line region. We find that this gas has a relatively low density of $n_e \sim 10^3$ cm$^{-3}$ and requires a relatively high ionisation parameter of $\log U \sim 1$.

(iii) We estimate the distance of the coronal line region in NGC 4151 from the central ionising source for the above gas density to be $\tau_{\rm lt} \sim 2.0$ light years. This value, which is well below the spatial resolution provided by current direct imaging results, puts this region well beyond the hot inner face of the obscuring dusty torus (of $\sim$ 2 light months). Together with the recombination time this results in a characteristic variability time scale of $\tau_{\rm var} \approx 2.2$ years, which is consistent with our main observational result that the coronal line gas emission has varied in an observing period of $\sim 8-11$ years, but only weakly so relative to the variability observed for the broad emission lines and hot dust emission.

(iv) Since the coronal line region requires a much higher ionisation parameter than the BELR, it cannot be part of a continuous gas distribution but is rather an independent entity. One possibility is that this region is a layer on the inner part of the dusty torus that becomes an efficient coronal line emitter only when evaporated in an X-ray heated wind (Pier & Voit 1995). We present tentative evidence for this scenario in the form of a temperature anti-correlation between the coronal line gas and hot dust, which indicates that the increased AGN radiation that heats the dusty torus appears to increase the cooling efficiency of the coronal line gas, most likely due to a stronger adiabatic expansion.

In a future paper, we plan to present a similar study of the coronal line variability for the well-known AGN NGC 5548.

## ACKNOWLEDGMENTS

We thank Jörg-Uwe Pott and Kirsten Schnülle for making their IRTF spectrum from 2010 available to us in electronic format. HL is supported by a European Union COFUND/Durham Junior Research Fellowship (under EU grant agreement number 267209). KCS thanks the astronomy group at Durham University for its hospitality during a collaborative visit supported by a Santander Mobility Grant. GJF acknowledges support by NSF (1108928, 1109061, and 1412155), NASA (10-ATP10-0053, 10-ADAP10-0073, NNX12AH73G, and ATP13-0153), and STScI (HST-AR-13245, GO-12560, HST-GO-12309, GO-13310.002-A, and HST-AR-13914), and to the Leverhulme Trust for support via the award of a Visiting Professorship at Queen's University Belfast (VP1-2012-025).

## REFERENCES

Appenzeller, I., & Oestreicher, R. 1988, AJ, 95, 45
Crenshaw, D. M., Kraemer, S. B., & George, I. M. 2003, ARA&A, 41, 117
Detmers, R. G., Kaastra, J. S., Costantini, E., McHardy, I. M., & Verbunt, F. 2008, A&A, 488, 67
Detmers, R. G., Kaastra, J. S., & McHardy, I. M. 2009, A&A, 504, 409
Erkens, U., Appenzeller, I., & Wagner, S. 1997, A&A, 323, 707
Fabricant, D., Cheimets, P., Caldwell, N., & Geary, J. 1998, PASP, 110, 79
Ferguson, J. W., Korista, K. T., & Ferland, G. J. 1997, ApJS, 110, 287
Ferland, G. J., Korista, K. T., Verner, D. A., Ferguson, J. W., Kingdon, J. B., & Verner, E. M. 1998, PASP, 110, 761
Filippenko, A. V. 1982, PASP, 94, 715
Gu, M. F., Holczer, T., Behar, E., & Kahn, S. M. 2006, ApJ, 641, 1227
Iserlohe, C., Krabbe, A., Larkin, J. E., Barczys, M., McElwain, M. W., Quirrenbach, A., Weiss, J., & Wright, S. A. 2013, A&A, 556, A136
Kaastra, J. S., et al. 2014, Science, 345, 64
Kaastra, J. S., Mewe, R., & Nieuwenhuijzen, H. 1996, in UV and X-ray Spectroscopy of Astrophysical and Laboratory Plasmas, ed. K. Yamashita & T. Watanabe, 411
Keenan, F. P., & Norrington, P. H. 1987, A&A, 181, 370
Kollatschny, W., Bischoff, K., Robinson, E. L., Welsh, W. F., & Hill, G. J. 2001, A&A, 379, 125
Komossa, S., et al. 2009, ApJ, 701, 105
Koshida, S., et al. 2014, ApJ, 788, 159
Koski, A. T. 1978, ApJ, 223, 56
Kraemer, S. B., et al. 2006, ApJS, 167, 161
Kraemer, S. B., Sharma, N., Turner, T. J., George, I. M., & Crenshaw, D. M. 2015, ApJ, 798, 53
Kramida, A., Yu. Ralchenko, Reader, J., & and NIST ASD Team. 2013, NIST Atomic Spectra Database (ver. 5.1), [Online]. Available: `http://physics.nist.gov/asd`. National Institute of Standards and Technology, Gaithersburg, MD.
Landt, H., Bentz, M. C., Ward, M. J., Elvis, M., Peterson, B. M., Korista, K. T., & Karovska, M. 2008, ApJS, 174, 282
Landt, H., Elvis, M., Ward, M. J., Bentz, M. C., Korista, K. T., & Karovska, M. 2011, MNRAS, 414, 218
Lodders, K., & Palme, H. 2009, Meteoritics and Planetary Science Supplement, 72, 5154
Mathews, W. G., & Ferland, G. J. 1987, ApJ, 323, 456
Mazzalay, X., Rodríguez-Ardila, A., Komossa, S., & McGregor, P. J. 2013, MNRAS, 430, 2411
Mullaney, J. R., Ward, M. J., Done, C., Ferland, G. J., & Schurch, N. 2009, MNRAS, 394, L16
Müller Sánchez, F., Davies, R. I., Eisenhauer, F., Tacconi, L. J., Genzel, R., & Sternberg, A. 2006, A&A, 454, 481
Müller-Sánchez, F., Prieto, M. A., Hicks, E. K. S., Vives-Arias, H., Davies, R. I., Malkan, M., Tacconi, L. J., & Genzel, R. 2011, ApJ, 739, 69
Murayama, T., & Taniguchi, Y. 1998, ApJ, 497, L9
Nelson, C. H., Weistrop, D., Hutchings, J. B., Crenshaw, D. M., Gull, T. R., Kaiser, M. E., Kraemer, S. B., &

Lindler, D. 2000, ApJ, 531, 257
Netzer, H. 1993, ApJ, 411, 594
Nussbaumer, H., Storey, P. J., & Storey, P. J. 1982, A&A, 113, 21
Oliva, E., Salvati, M., Moorwood, A. F. M., & Marconi, A. 1994, A&A, 288, 457
Osterbrock, D. E. 1977, ApJ, 215, 733
Osterbrock, D. E., & Ferland, G. J. 2006, Astrophysics of Gaseous Nebulae and Active Galactic Nuclei (University Science Books)
Pelat, D., Alloin, D., & Bica, E. 1987, A&A, 182, 9
Penston, M. V., Fosbury, R. A. E., Boksenberg, A., Ward, M. J., & Wilson, A. S. 1984, MNRAS, 208, 347
Pier, E. A., & Voit, G. M. 1995, ApJ, 450, 628
Porquet, D., & Dubau, J. 2000, A&AS, 143, 495
Porquet, D., Dumont, A.-M., Collin, S., & Mouchet, M. 1999, A&A, 341, 58
Porter, R. L., & Ferland, G. J. 2007, ApJ, 664, 586
Pounds, K. A., & Page, K. L. 2005, MNRAS, 360, 1123
Prieto, M. A., Marco, O., & Gallimore, J. 2005, MNRAS, 364, L28
Rayner, J. T., Toomey, D. W., Onaka, P. M., Denault, A. J., Stahlberger, W. E., Vacca, W. D., Cushing, M. C., & Wang, S. 2003, PASP, 115, 362
Riffel, R., Rodríguez-Ardila, A., & Pastoriza, M. G. 2006, A&A, 457, 61
Rodríguez-Ardila, A., Prieto, M. A., Portilla, J. G., & Tejeiro, J. M. 2011, ApJ, 743, 100
Rodríguez-Ardila, A., Viegas, S. M., Pastoriza, M. G., & Prato, L. 2002, ApJ, 579, 214
Schnülle, K., Pott, J.-U., Rix, H.-W., Decarli, R., Peterson, B. M., & Vacca, W. 2013, A&A, 557, L13
Steenbrugge, K. C., et al. 2005, A&A, 434, 569
Steenbrugge, K. C., Kaastra, J. S., de Vries, C. P., & Edelson, R. 2003, A&A, 402, 477
Storchi-Bergmann, T., McGregor, P. J., Riffel, R. A., Simões Lopes, R., Beck, T., & Dopita, M. 2009, MNRAS, 394, 1148
Veilleux, S. 1988, AJ, 95, 1695
Wang, J., et al. 2011a, ApJ, 742, 23
Wang, J., Fabbiano, G., Elvis, M., Risaliti, G., Mundell, C. G., Karovska, M., & Zezas, A. 2011b, ApJ, 736, 62
Witthoeft, M. C., & Badnell, N. R. 2008, A&A, 481, 543
Yang, C.-W., Wang, T.-G., Ferland, G., Yuan, W., Zhou, H.-Y., & Jiang, P. 2013, ApJ, 774, 46
Zu, Y., Kochanek, C. S., & Peterson, B. M. 2011, ApJ, 735, 80

This paper has been typeset from a TEX/ LATEX file prepared by the author.